RSC Advances

PAPER

View Article Online
View Journal | View Issue

Check for updates

Cite this: *RSC Adv.*, 2025, **15**, 38532

Solid-state *in situ* synthesis of g-C_3N_4/ZnO nanocomposites for photocatalytic water cleaning

Adina Zholdas,[ab] Abylay Abilkhan,[b] Islam Rakhimbek,[b] Oleg Rofman,[c] Daniyar Salikhov,[d] Fail Sultanov[b] and Batukhan Tatykayev*[ab]

Received 28th August 2025
Accepted 3rd October 2025

DOI: 10.1039/d5ra06422h

rsc.li/rsc-advances

We present a scalable, solvent-free two-step route to g-C_3N_4/ZnO heterostructured nanocomposites for solar-driven wastewater remediation. g-C_3N_4 is first obtained by conventional thermal polymerization of melamine; in the second step, ZnO is introduced mechanochemically, yielding intimate g-C_3N_4/ZnO interfacial contact and robust heterojunctions. Composites with 2–20 wt% g-C_3N_4 were synthesized and comprehensively characterized. The optimized ZOCN10 (10 wt% of g-C_3N_4) exhibits rate constant $k = 0.0389\ \text{min}^{-1}$ and achieves ~95% methylene blue removal within 90 min under simulated solar irradiation, outperforming both pristine ZnO and g-C_3N_4 4.6 and 5.5 times, respectively and clearly surpassing a physical mixture. Reactive-species trapping indicates h^+ and O_2^- as the dominant actors in the degradation pathway. The catalyst remains reusable across multiple cycles, retaining a substantial portion of its activity and thereby supporting practical deployment scenarios in water treatment. By eliminating organic solvents while enabling scalable processing and efficient solar-light operation, this mechanochemically assisted approach provides a green and cost-effective path to high-performance photocatalysts for wastewater purification.

1. Introduction

Environmental pollution is one of most serious problems that people face nowadays. Researchers are looking for the most environmentally friendly and sustainable solutions to tackle this issue[1] Photocatalysis is attracting more and more attention and has proven to be a promising technology for solving many environmental problems.[2,3] There are several interesting applications of this technology, such as the conversion of solar energy into chemical energy, hydrogen production by photocatalytic decomposition of water,[4–6] reduction of CO_2,[7,8] creation of nanosensors,[9] decomposition of pollutants in water and other areas.[10–12] A wide range of organic dyes originating from industries such as printing, textiles, cosmetics, and food processing represent major contaminants of both aquatic and terrestrial environments. Due to their high toxicity and resistance to biodegradation, these dyes pose serious risks to human health and aquatic ecosystems. Traditional physical and chemical methods, such as adsorption and nanofiltration, cannot completely decompose dyes, and can also lead to the formation of secondary pollutants.[1,13,14] In comparison, photocatalytic degradation is a more efficient and environmentally friendly method for removing organic dyes from wastewater.[15] Therefore, the development of new photocatalytic materials is relevant today.[16,17]

Zinc oxide is probably the most promising material for creating photocatalytic structures, as it has a number of advantages, namely, high photosensitivity, temperature and mechanical stability, and low reflection coefficient.[18] In addition, ZnO does not harm the environment, and the low cost of precursors opens up the possibility of adapting the technology for industrial applications.[19] As of now, existing photocatalysts based on ZnO are active mainly in the ultraviolet range of the spectrum.[20,21] It poses the most urgent task for developing new oxide catalysts with an advanced set of properties in the visible spectrum. One of the known methods of shifting the spectral range of the catalytic action of zinc oxide and increasing the yield of reactions is its doping with other transition elements, such as vanadium, iron, cobalt, nickel, as well as sulfur, carbon, and nitrogen.[22,23] The development of a heterostructured photocatalyst in combination with ZnO and other compatible semiconductors is an effective strategy for extending the service life of free charges and increasing photocatalytic activity.[24–27]

Over the past few years, the graphite-like semiconductor g-C_3N_4 has become an attractive alternative for various scientific applications.[28] Graphite-like carbon nitride (g-C_3N_4) is an inorganic polymeric semiconductor with a relatively narrow

---

[a] *Department of General and Inorganic Chemistry, Al-Farabi Kazakh National University, 050040, Almaty, Kazakhstan. E-mail: batukhan.tatykayev@nu.edu.kz*

[b] *National Laboratory Astana, Nazarbayev University, Kabanbay Batyr Ave., 53, Astana, 010000, Kazakhstan*

[c] *Laboratory of Radiation Materials Science, Institute of Nuclear Physics, 050032, Almaty, Kazakhstan*

[d] *Department of Inorganic Chemistry, Eötvös Loránd University, Egyetem tér 1-3, 1053 Budapest, Hungary*

band gap of 2.72 eV,[29,30] making it well-suited for the absorption of visible light.[31] g-C_3N_4 can also be readily doped or chemically modified to tailor its photophysical properties. Compared to many other organic semiconductors, graphite carbon nitride has a high thermal and chemical resistance to oxidation even at a temperature of 500 °C.[32,33] Since its introduction, graphite carbon nitride has gained widespread popularity in the field of photocatalysis and is frequently incorporated with other semiconductors to enhance overall performance.[34,35] A successful synthesis of the g-C_3N_4/ZnO composite material would make ZnO-based catalysts a promising development since g-C_3N_4 can both expand the spectral response range and reduce the recombination rate of electron–hole pairs.[7,36,37] Recent reports confirm this relevance on a practical scale, showing the efficient photodegradation of persistent pollutants under simulated solar irradiation and emphasizing the need for visible-light-active catalysts.[38] In line with this trend, the g-C_3N_4/ZnO composites developed in this work also exhibit high activity under solar light irradiation, further confirming their potential for practical environmental applications.

Preparation methods of g-C_3N_4/ZnO nanocomposites have been studied in detail and collected in Table S1, given in the SI. It summarizes how the main parameters of the nanocomposite's preparation, such as the reagents used, the ratio of semiconductors in the composition of nanocomposites, morphology, and the use of nanocomposites as a photocatalyst for water purification vary across the literature. All methods were classified into three strategy groups, with the description and the main advantages and disadvantages of each group shown using an illustrative diagram in Fig. 1.

The main application for these composites is photodegradation of organic pollutants. Other applications include the production of hydrogen and the reduction of CO_2 emissions. For example,[39] recently reported a flash Joule heating strategy to obtain nitrogen-rich defective g-C_3N_4. This solvent-free and energy-efficient method provided precise defect engineering, and after Pt co-decoration, enabled outstanding hydrogen evolution activity. This study underlines the current trend of developing green and scalable synthetic routes for photocatalysts. In our case, the approach is different: g-C_3N_4 is first obtained by conventional thermal polymerization of melamine, and in a second step, ZnO is introduced through a mechanochemical process.

In summary, while recent studies have highlighted the importance of sustainable synthetic strategies for g-C_3N_4-based photocatalysts, our work introduces a novel two-step approach that integrates thermal polymerization with mechanochemical processing to obtain g-C_3N_4/ZnO composites. The key innovation lies in the solvent-free and scalable mechanochemical step, which promotes intimate interfacial contact between the components and results in enhanced photocatalytic activity sustained over multiple reuse cycles. Notably, this study provides the first demonstration of the *in situ* mechanochemical growth of ZnO directly on g-C_3N_4. The process is rapid, energy-efficient, and operates under low-temperature calcination, thereby improving scalability and environmental compatibility. Furthermore, the resulting nanosized composites with strong interfacial coupling exhibit significantly enhanced photocatalytic efficiency and stable performance over at least four consecutive cycles, underscoring the potential of this green and industrially adaptable strategy for practical photocatalytic applications.

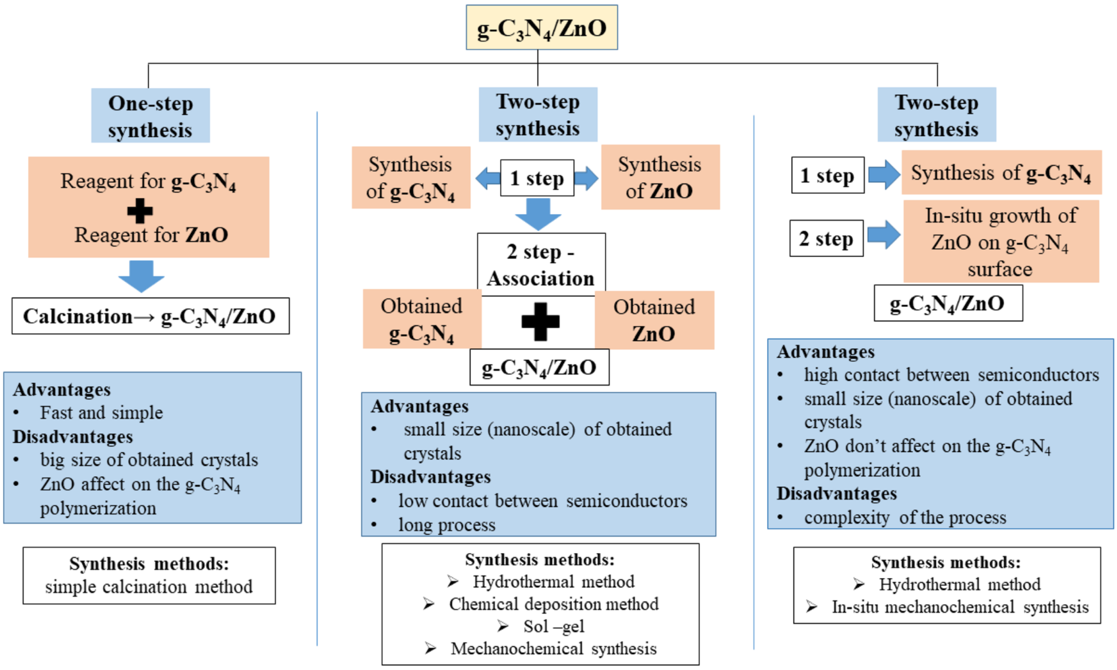

Fig. 1 Clarifying differences between nanocomposites production methods.

2. Experimental part

2.1 Materials

Zinc acetate dihydrate (Zn $(CH_3COO)_2 \cdot 2H_2O$), melamine ($C_3H_6N_6$ 99.0%), urea (CH_4N_2O 99.0%), methylene blue (MB) organic dye and anhydrous ethanol (C_2H_5OH) were purchased from Sigma-Aldrich. Deionized water was produced using YA-ZD series electric distillator.

2.2 g-C_3N_4 preparation

The graphitic carbon nitride was obtained by thermopolymerization of melamine and urea solid mixture. 5 g melamine and 5 g urea were mixed in agate mortar, and calcined in a muffle furnace in a porcelain crucible for 2 hours at 550 °C. After calcination, the product was allowed to cool down to room temperature. The resulting yellow solid product (3.72 g) was ground in an agate mortar for the next step.

2.3 *In situ* mechanochemical synthesis of $Zn(OH)_2$ on g-C_3N_4 sheets

Zinc acetate dihydrate was dried in an oven at 100 °C for 2.5 hours. 2.25 g of dry zinc acetate and 0.02 g of g-C_3N_4 were placed in the bowl, and mechanically activated by using activator – 2SL planetary ball mill (Russia) for mechanical alloying/activation for 10 minutes. Next, 0.98 g of sodium hydroxide was added to a bowl and mechanical activation (MA) was continued for 10 more minutes. The final product was washed 3 times with DI water and dried at 60 °C for 12 hours. Mechanochemical synthesis was performed in a silicon nitride (Si_3N_4) bowl (80 mL) using Si_3N_4 balls (d = 10 mm, m = 1.8 g, 18 pcs). The milling speed was set to 360 rpm under water cooling at 10 °C. The ball-to-reagent mass ratio was maintained at 10 : 1, and the activation time was 10 min.

2.4 Thermal conversion of g-C_3N_4/$Zn(OH)_2$ to g-C_3N_4/ZnO

g-C_3N_4/$Zn(OH)_2$ was placed in ceramic crucible and calcined in a muffle furnace at 150 °C for 1 hour to convert $Zn(OH)_2$ to ZnO. Obtained nanocomposites had mass ratio of g-C_3N_4 – 2% and ZnO – 98%. Samples with different g-C_3N_4/ZnO ratios were prepared by a similar method. The weight contents of g-C_3N_4 in the photocatalysts were 2, 5, 10 and 20 wt%. For simplicity reason, the composites were named ZOCN2, ZOCN5, ZOCN10 and ZOCN20, respectively. For a comparative study, pure zinc oxide was obtained by a similar mechanochemical method.

2.5 Catalyst characterization

The structural and phase composition of the synthesized nanocomposites was analyzed using Powder X-ray Diffraction (XRD) with a MiniFlex 300/600 diffractometer equipped with Cu Kα radiation, operating at 40 kV and 15 mA. Data were collected over a 2θ range of 3°–90° with a step size of 0.02° and an acquisition time of 1 second per step.

Fourier-transform infrared (FT-IR) spectroscopy was used to analyze the chemical bonds and surface functional groups of the samples. The measurements were performed with a PerkinElmer Spectrum 65 spectrometer over the wavenumber range of 4000 to 450 cm^{-1} with a spectral resolution of 4 cm^{-1}.

The structure and elemental composition of the samples were determined with the help of a pacified ion-electronic microscope Quanta 200i 3D (FEI Company, USA). The image of the surface area of the coatings is obtained with the use of a secondary electron detector, which has a large lateral resolution of up to 3.5 nm.

High-resolution microstructural analysis was conducted using a JEM-2100 transmission electron microscope (JEOL, Japan) operated at an accelerating voltage of 200 kV and equipped with an X-Max energy-dispersive X-ray spectroscopy (EDS) detector from Oxford Instruments (UK).

The UV-vis absorption spectra were measured using a Shimadzu 2600i spectrophotometer to investigate the optical absorption characteristics of the samples and estimate their band gap energies.

Chemical, electronic states of the atoms and the elemental composition was determined by the X-ray photoelectron spectroscopy (XPS) analysis. The procedure was carried out on the NEXSA X-ray photoelectron spectrometer (Thermo Scientific, USA) having a double-focusing, hemispherical analyzer with 128 channel detector. The X-ray source type was monochromated low power Al Ka X-ray source – 1486.6 eV. Additionally, Ultraviolet Electron Spectroscopy (UPS) was an add-in to the XPS analysis to measure the kinetic energy spectra of photoelectrons caused by ultraviolet photons absorption by molecules and to estimate the molecular orbital energies in the valence region.

Photoluminescence (PL) spectra were obtained using a spectrofluorimeter with a SOLAR CM 2203 xenon lamp (Belarus). The permissible absolute error limits of the excitation and emission monochromator wavelength settings were $\pm$1.0 nm.

2.6 Photocatalytic experiment

To evaluate the photocatalytic activity of the nanocomposites, an aqueous methylene blue (MB) solution with a concentration of 10 mg L^{-1} was used as a model system. A total of 20 mg of catalyst was added to 40 mL of the MB solution. The suspension was ultrasonicated for 3 minutes to ensure thorough dispersion. Before irradiation, the mixture was stirred for 60 minutes in the dark using a magnetic stirrer to determine the adsorption–desorption equilibrium of the dye on the catalyst surface. Solar light irradiation was provided by an Osram Vita-Lux 300 W lamp, with an intensity of 15 mW cm^{-2} for all experiments. During the reaction, 2 mL aliquots of the suspension were withdrawn every 30 minutes. Nanoparticles were separated from the collected samples by centrifugation at 10 000 rpm. The photocatalytic degradation rate of MB was monitored by measuring the temporal changes in the absorption spectrum at 665 nm using an SF-56 spectrophotometer. For comparison, the photocatalytic activities of pure ZnO and g-C_3N_4 were also evaluated following the same experimental procedure.

Furthermore, the stability of the photocatalysts was evaluated through four consecutive cycles of MB dye decolorization.

After each cycle, the catalyst was collected, washed with deionized water, and reused in the subsequent experiment.

3. Results and discussion

3.1 Solid-state synthesis of g-C_3N_4/ZnO nanocomposites

To prepare g-C_3N_4 a melamine-urea binary route was chosen, because mixed precursors reproducibly yield g-C_3N_4 with higher porosity/surface area and superior activity *versus* single-precursor analogues.[40] Composition-activity trends for melamine/urea mixtures have also been mapped specifically for gas-phase formaldehyde removal. The optimal fraction of urea provides a higher mineralization rate compared to single-precursor samples, which is attributed to the increased porosity and more favorable surface chemistry.[41] Using a binary urea-melamine precursor over a single component to achieve superior texture and photocatalytic activity.[42]

g-C_3N_4/ZnO nanocomposites were successfully prepared by using mechanochemical route with subsequent thermal treatment. Schematic illustration of g-C_3N_4/ZnO nanocomposites preparation is shown in Fig. 2.

3.2 Characterization of samples

Powder X-ray diffraction (XRD) was applied to characterize the phase composition and purity of the samples. The XRD patterns (Fig. 3a–c) confirm wurtzite ZnO together with layered g-C_3N_4. Pristine g-C_3N_4 displays the interlayer (002) reflection at 2θ 27.5° (interplanar spacing $d_{002} \approx 0.326$ nm),[8,43] characteristic of the graphite-like stacking; a weak (100) near ≈13° may appear depending on crystallinity.[44] Pristine ZnO shows the hallmark reflections at 31.7° (100), 34.4° (002), 36.2° (101), 47.5° (102), 56.6° (110), 62.8°(103) and 68.0° (112) of the hexagonal wurtzite phase (ICDD 00-036-1451).[9,45,46] All ZOCN composites (ZOCN2/5/10/20) are indexed by the same ZnO card (ICDD 00-036-1451). No impurity reflections are observed. With increasing g-C_3N_4 loading, the intensity of the 27.5° reflection increases (Fig. 3c),[47] while the ZnO peak positions remain unchanged, indicating no lattice-parameter change.

FT-IR spectra can give abundant structural information about g-C_3N_4/ZnO nanocomposites. In the FT-IR spectrum (Fig. 3d) the characteristic peak at 450 cm^{-1} corresponds to the stretching vibration of the Zn–O bond.[48,49] As for the pure g-C_3N_4, peaks in the range of 1200–1620 cm^{-1} (1247.25 cm^{-1}, 1318.0 cm^{-1}, 1413.66 cm^{-1} and 1631.21 cm^{-1}) refer to the typical stretching vibration of CN heterocycles (the bands of C=N, C–N) and demonstrate the presence of g-C_3N_4 in composites.[50,51] The sharp peak at 809.25 cm^{-1} is attributed to the breathing vibration of triazine units, revealing that the local structure of the obtained g-C_3N_4 is composed of triazine units.[52] The broad absorption band at 3000–3600 cm^{-1} indicates the presence of NH_2 or NH functional groups in the aromatic ring of g-C_3N_4.[8,53]

SEM images and related EDS spectra were made to investigate the structure of obtained composites and of pure ZnO and g-C_3N_4 (Fig. 4). The image of pure graphitic carbon nitride shows a clearly defined structure in the form of separate layers with the size of 1–2 μm (Fig. 4b), while the size of obtained ZnO is about 50–100 nm (Fig. 4a). The composite images show that small agglomerations of zinc oxide only partially are located on the surface of the g-C_3N_4 layers (Fig. 4c and d). Compared to pure ZnO, the size of the composites is larger and the size distribution is not uniform. This is due to the particles increase in size during the heat treatment of the samples. The diameter of ZOCN5 and ZOCN10 composites varies in the range of 100–200 nm.

The chemical element composition of the samples was determined by EDX analysis (Fig. S1 and Table 1). According to the results of EDX analysis[10] the weight percentage of Zn and O elements present in the sample, in the form of pure ZnO is 89.83 and 10.17 wt% and the weight percentage of C and N in the form of g-C_3N_4 is 37.97 and 62.03 wt% respectively. In case of composites, the presence of all four elements is observed, most of which account for O and Zn with the weight percentage of 15.07, 63.42 wt% for ZOCN5 and 14.28, 62.91 wt% for ZOCN10, respectively. This indicates the successful *in situ* synthesis of composites.

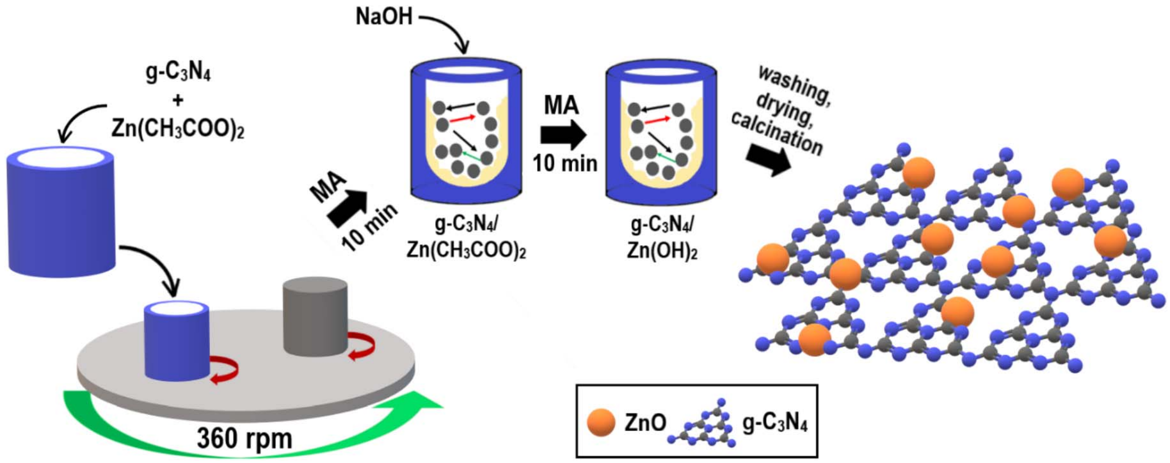

Fig. 2 Schematic illustration of the synthesis of g-C_3N_4/ZnO photocatalysts.

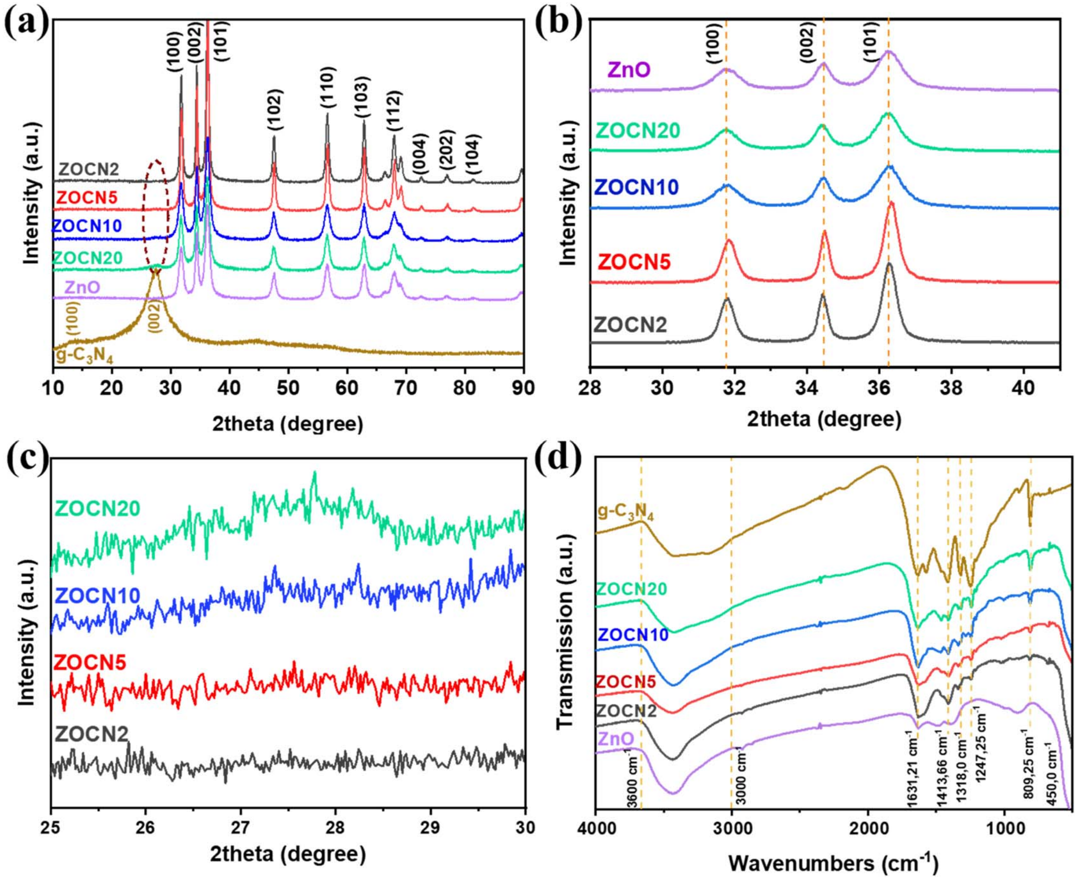

Fig. 3 XRD patterns (a–c) and FT-IR spectra (d) for composites ZOCN2, ZOCN5, ZOCN10, ZOCN20 and for pure ZnO, g-C_3N_4.

The detailed morphology and structure of the ZOCN10 composite were investigated by TEM analysis (Fig. 5). The TEM images (Fig. 5a–c) reveal stacked and interlinked g-C_3N_4 lamellae decorated with darker ZnO nanoparticles distributed across the nanosheets, which is consistent with the SEM observations. The contrast between light and dark regions arises from the overlapping g-C_3N_4 layers and the higher electron density of ZnO, respectively. The SAED pattern (Fig. 5d) exhibits concentric rings indexed to the (100), (002), (102), (110), (103) and (200) planes of wurtzite ZnO (ICDD 00-036-1451) confirming its crystallinity. High-resolution TEM (Fig. 5 e,f) further demonstrates well-defined lattice fringes at the g-C_3N_4/ZnO interface; the measured interplanar distance of ∼0.521 nm corresponds to [0001] direction of wurtzite ZnO, in agreement with literature values.[54] Complementary EDS elemental mapping (Fig. 6) confirms the co-localization of Zn and O signals, consistent with ZnO nanoparticles, while C and N signals outline the g-C_3N_4 framework. The corresponding EDS spectrum (Fig. 7) further verifies the presence of Zn, O, C and N without extraneous impurities; the detected Cu peak originates from the TEM grid. Together, these observations confirm that crystalline ZnO nanoparticles are firmly anchored on layered g-C_3N_4, providing intimate heterointerfaces that are expected to facilitate charge separation and transfer in photocatalytic processes.

The surface element distribution and chemical binding status of the g-C_3N_4/ZnO nanoparticles was investigated *via* XPS analysis. A constant binding shift was not applied to spectra obtained in each batch since no significant charge correction to the adventitious carbon C 1s was needed. Fig. 8a shows the XPS survey spectra with mainly Zn, C, N, O elements without impurities. High-resolution Zn 2p spectrum (Fig. 8b) revealed two intense peaks at 1049.20 eV and 1026.30 eV assigned to the Zn $2p_{1/2}$ and Zn $2p_{3/2}$ peaks of ZnO, correspondingly. Likewise, these peaks demonstrated considerable reduction in intensity with slight downshifts in binding energy after binding with g-C_3N_4. Decreased intensity behavior, additionally, points at the significantly decreased electronic density of ZnO during the heterojunction formation. A sub-peak risen at 1021.80 eV is attributed to the Zn–N bond (Fig. 8b).[55] The XPS data of the C 1s spectrum revealed multiple peaks, in which peaks at 284.48 eV, 287.88 eV, and 289.09 eV correspond to carbon atoms in sp^2 hybridization, while other two correspond to carbon atoms bonded with nitrogen groups linking different rings. Other three peaks of the C 1s spectrum at 291.48 eV, 292.28 eV, and 292.88 eV are attributed to oxidized states and correspond to C–O–N, C–OH, and C–O–Zn bonds (Fig. 8c).[56] The N 1s spectrum showed four binding peaks at 398.38 eV, 400.88 eV, 403.08 eV, and 405.08 eV. The dominant nitrogen peak at 403.08 eV is assigned at sp^2 hybridized pyridinic nitrogen atoms linked with

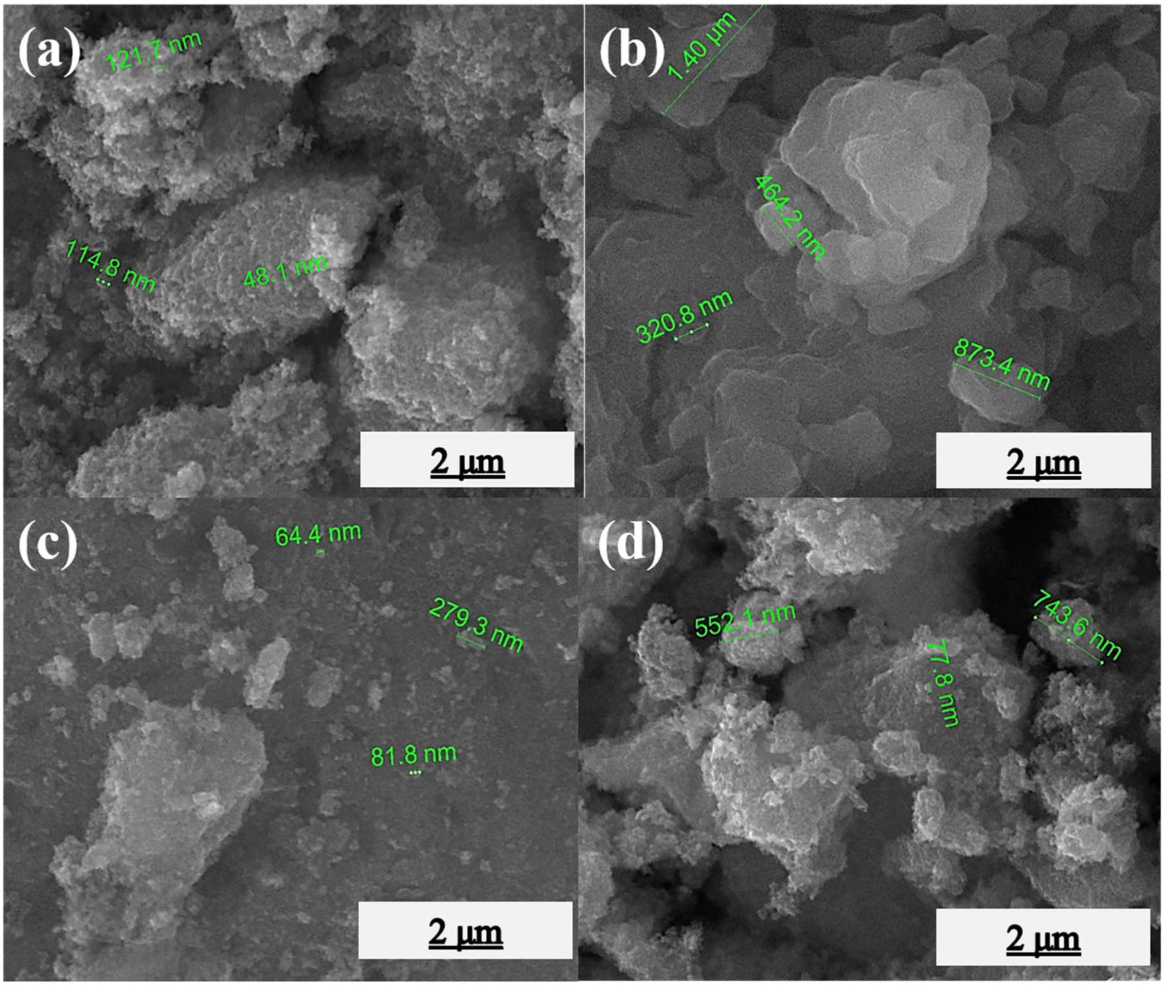

Fig. 4 SEM images of ZnO (a), g-C_3N_4 (b) and ZOCN5 (c), ZOCN10 (d) composite.

Table 1 The chemical elemental composition by EDX

	g-C_3N_4		ZnO		ZOCN5		ZOCN10	
Element/sample	wt%	at%	wt%	at%	wt%	at%	wt%	at%
C	37.97	41.65	—	—	17.45	41.55	17.13	38.68
N	63.02	58.35	—	—	1.50	3.07	5.68	11.01
O	—	—	10.17	31.63	15.07	26.94	14.28	24.21
Zn	—	—	89.83	68.37	63.42	27.75	62.91	26.11

two carbon atoms (C–N=C). The peak at 400.88 eV originates from triazine groups (C=N–H). The peak at 405.08 eV is attributed to tertiary nitrogen groups N–$(C)_3$ forming graphitic-like structure and bridged network. The last nitrogen peak at 398.38 eV corresponds to the quaternary nitrogen, which replaces a carbon atom in the graphene layer with subsequent incorporation to that structure. Furthermore, this peak can be correlated to the Zn–N bonding as a proof that nitrogen from the supporting material is chemical bonded with zinc in ZnO, which makes the heterojunction more stable and effective (Fig. 8d).[57,58] It should be noted that the overall binding energy of C 1s and N 1s spectrums upshifted after heterojunction of ZnO with g-C_3N_4 due to redistribution of electronic states and density.[57,59] The O 1s spectrum detected four binding peaks at 531.18 eV, 533.78 eV, 535.98 eV, and 537.48 eV corresponding to g-C_3N_4/ZnO, Zn–O–N, Zn–O, and O–H states, additionally, confirming the presence of ZnO on the surface of g-C_3N_4 (Fig. 8e).[56,60] The Zn LMM Auger spectra was observed from the XPS survey to scan the presence of Zn_i defects in the g-C_3N_4/ZnO composite (Fig. 8f). According to the Fig. 8e, Zn LMM Auger spectra showed two peaks corresponding to the interstitial site at 479.70 eV and the peak of the lattice site (Zn–O bond) at 503.10 eV of binding energy that deconvoluted into three sub-peaks at 497.10 eV, 500.10 eV, and 503.20 eV of binding

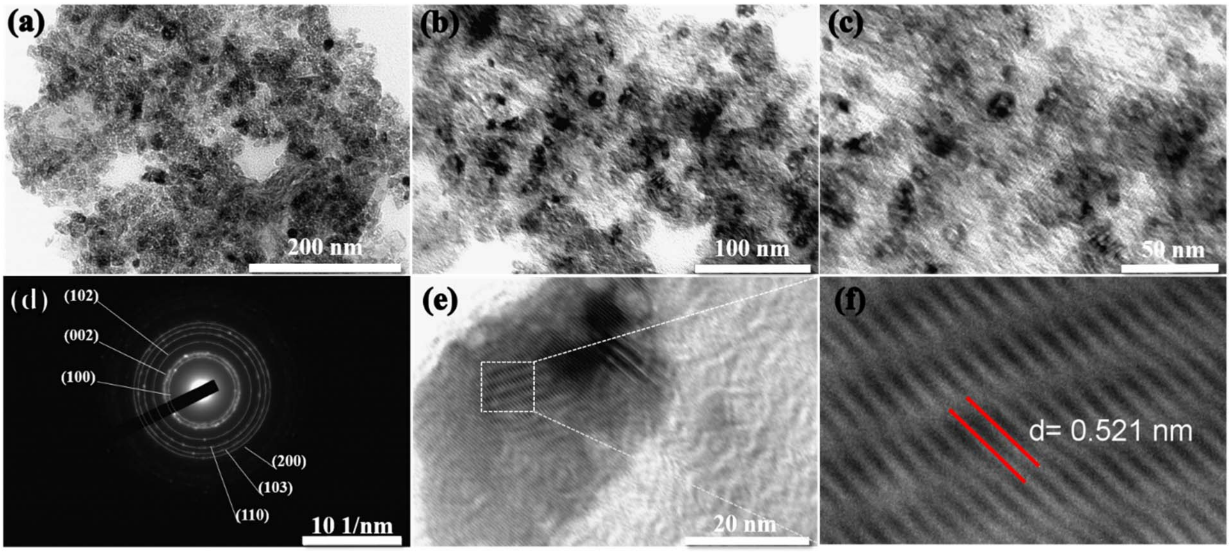

Fig. 5 TEM images of ZOCN10 (a–c), SAED patterns (d), HR-TEM images of ZOCN10 (e and f).

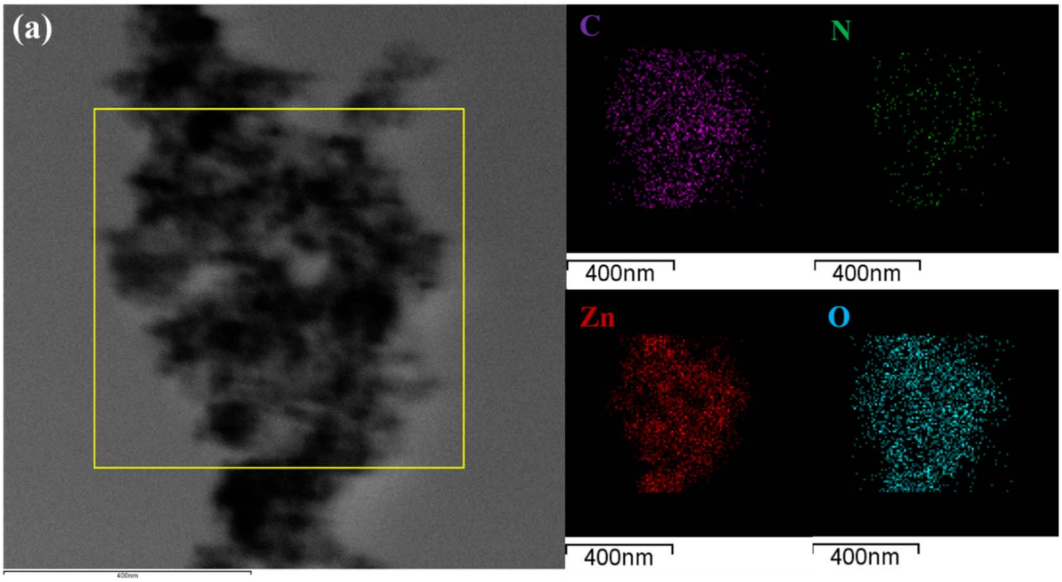

Fig. 6 EDS elemental mapping ZOCN10 nanocomposites (a).

energies, respectively. The intensity of these two main peaks point at the extent of Zn_i defects in the composite. The intensity between the lattice and interstitial sites indicated insignificant difference, thus, the defects concentration of Zn_i in the Zn–O bond was identified with minor amounts and having no substantial effect on the composites structure, overall.[61]

The UPS spectra (Fig. 8g) was employed to calculate the valence band energy/maximum (E_v or VBM) of the ZOCN10 composite, which was identified to be 1.32 eV and in line with ordinary g-C_3N_4 band maximum positions.

The optical properties of the obtained samples were studied with the help of UV-vis absorption and were recorded in the wavelength range of 300–700 nm as shown on the Fig. 8(h). For pure ZnO the absorption edge was observed at ~375 nm and for g-C_3N_4 this value was at ~460 nm, which is consistent with the previous study.[62] With an increase of concentration of zinc oxide in the composite, a shift towards shorter waves is observed. The synthesized composites exhibit optical properties identical to pure zinc oxide. The absorption curves of ZnO and ZOCN composites had a similar pattern with a sharp absorption edge but differed significantly from the absorption curve of g-C_3N_4.This indicates that the mechanochemical synthesis enables the formation of strong contact between the components of the nanocomposites.[63] The band gap of samples was determined by following equation (Tauc plot) (1).

$$(\alpha h\nu)^2 = A(h\nu - E_g) \tag{1}$$

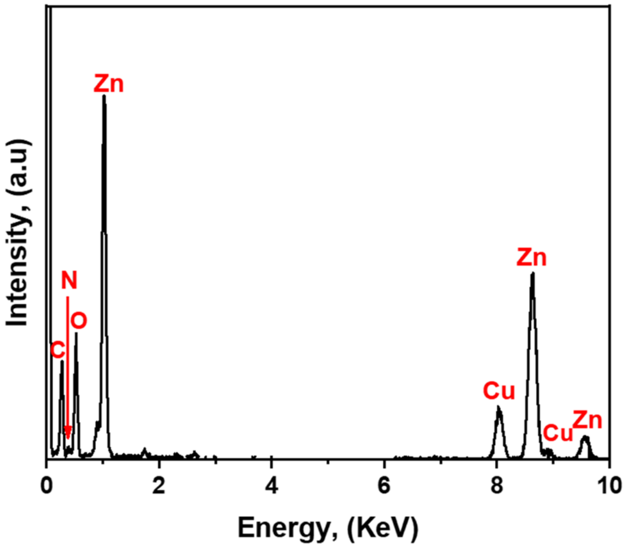

Fig. 7 TEM EDS spectrum of ZOCN10.

Table 2 Band gap values of synthesized catalysts

Catalyst	ZnO	ZOCN2	ZOCN5	ZOCN10	ZOCN20	g-C_3N_4
Band gap	3.21 eV	3.10 eV	3.04 eV	2.98 EV	2.92 eV	2.76 eV

where α is absorption coefficient, h is Planck's constant, ν is the incident photon frequency, A is constant and E_g is a band gap respectively. The band gaps of the photocatalysts were estimated from the intersection points of the tangents on the $(\alpha h\nu)^2$ *versus* photon energy ($h\nu$) plots, as illustrated in Fig. 8(i). The estimated band gaps range from 2.92 to 3.10 eV for ZOCN composites, intermediate between ZnO (3.21 eV) and g-C_3N_4 (2.76 eV) (Table 2). Increasing the concentration of carbonitride in the composite leads to a decrease in its band gap. The decrease of E_g value in the composites is explained by the effective interaction of the components of the ZOCN composites, thereby improving their properties. Thus, obtained valence band energy E_v and band gap E_g can help us determine the

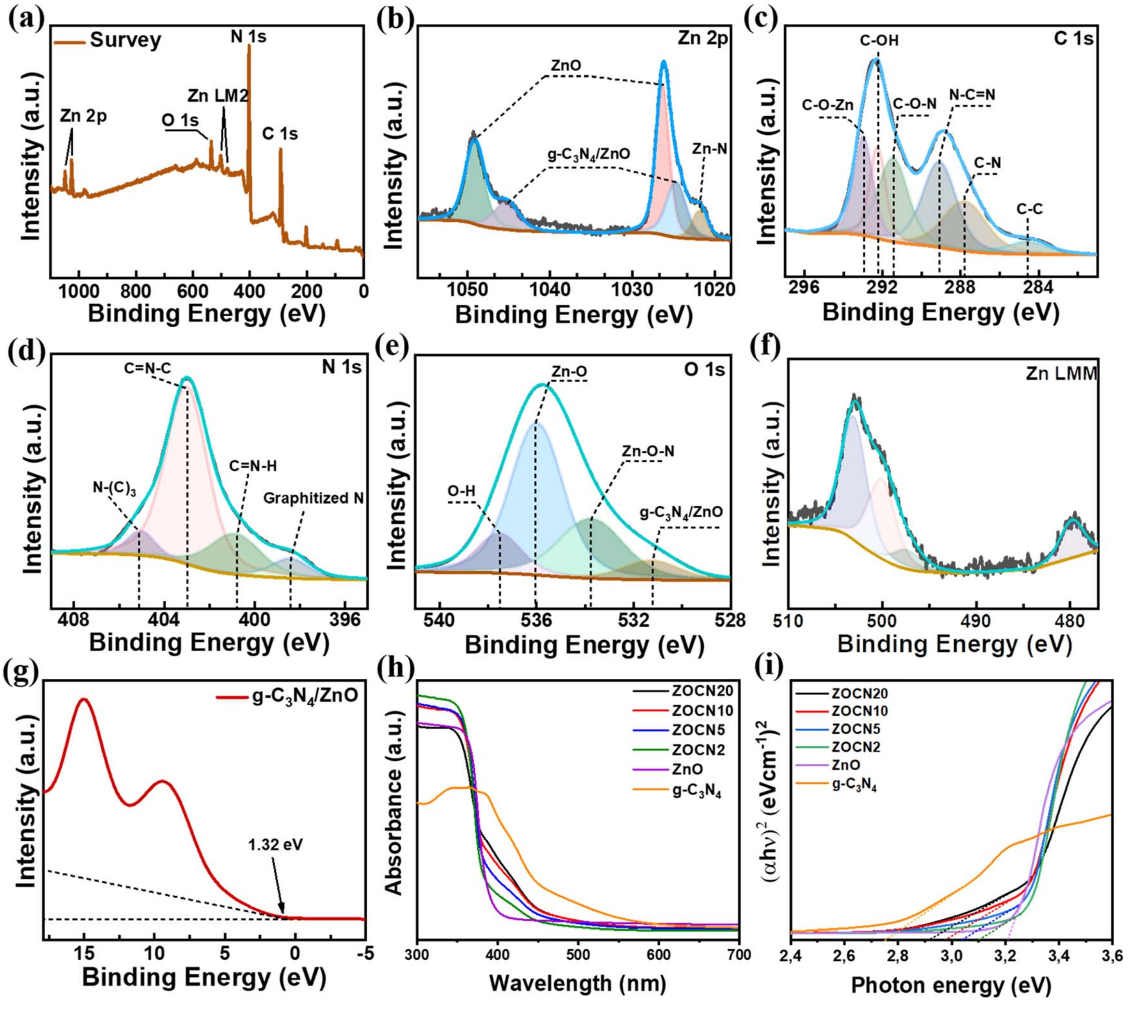

Fig. 8 XPS survey spectra of the ZOCN10 (a), high resolution spectra of Zn 2p, C 1s, N 1s, O 1s, Zn LMM (b–f), UPS spectrum (g), UV-vis absorption spectra (h) and Plots of the $(\alpha h\nu)^2$ *versus hν* photon energy for synthesized samples (i).

conduction band minimum (CBM). As the E_v of ZOCN10 was revealed to be 1.32 eV, subsequently, the CBM can be found *via* the following formula:

$$\mathrm{CBM} = E_g - E_v \tag{2}$$

Therefore, the CBM of ZOCN was calculated to be 1.66 eV and above the Fermi level. The importance of this finding implies the occurrence of band bending. In other words, photogenerated electrons in g-C_3N_4 moved into the CBM of ZnO, while since standard VBM of ZnO ($\sim$2.60 eV) is more positive, holes in ZnO moved to the carbonitride instead. As a result of this, it is evident that a type II heterojunction had been formed, and the material is behaving as a composite now than just two separate chemicals. The benefits of this are improved photocatalytic activity (owing to reduced recombination) and stronger physico-chemical interface. More precisely, in detected Zn–N bonds according to XPS results, electron transfer becomes even more efficient thanks to the direct Zn-to-N interactive pathways. The revealed outcomes are vital for the durability of the ZOCN composite because chemical bonding makes sure that the material is less likely to be easily dissolved or photocorroded. Thus, this provides the ZOCN composite with newer attributes like durability and efficient activity over many recycling cycles.

The spectral features of ZOCN10 composite (Zn^{2+} doublet in Zn 2p, heptazine-related C 1s and N 1s, defect-related O 1s, and band gaps of 2.92–3.10 eV) are in good agreement with previous reports on bio-capped ZnO/g-C_3N_4 nanocomposites.[64] In both cases, the optical absorption profile remains ZnO-like, indicating that the enhanced activity arises from interfacial charge separation rather than band-gap narrowing.

The photoluminescence spectrum (PL) is a useful tool to evaluate the recombination of e^- h^+ pairs in synthesized samples as illustrated in Fig. 9. The PL spectrum of g-C_3N_4 exhibits a broad intense band with a maximum at $\sim$450 nm and a defect-related shoulder in the 500–550 nm region (Fig. 9a) Due to the much higher signal of g-C_3N_4, the signals of ZnO and the composites in the 400–500 nm range are not distinguishable on the same scale and are therefore shown separately in an enlarged view in Fig. 9b. The increase in peak intensity of the composites relative to ZnO originates from the contribution of g-C_3N_4, whereas compared to g-C_3N_4 a quenching of emission is observed. The ZnO-related peak at 600 nm in the composite disappeared. This PL change indicates more efficient charge separation and suppression of recombination.[65,66] These findings are corroborated by photocatalytic tests, where the best activity is achieved for the ZOCN10 composite.

In summary, the structural, morphological, and spectroscopic analyses demonstrate that ZnO nanoparticles are homogeneously anchored on layered g-C_3N_4 with strong interfacial interactions, as confirmed by TEM/EDS and XPS. The optical band gaps of 2.92–3.10 eV and the measured VBM position suggest efficient charge excitation and migration under solar light. Such features are beneficial for suppressing carrier recombination and activating surface redox processes. Therefore, the obtained composites are promising photocatalysts, and their photocatalytic performance was subsequently investigated under solar irradiation.

3.3 Photocatalytic activity of samples

The adsorption capacity of each powder was determined using methylene blue (MB) as a model dye. MB was selected due to its high optical density at 665 nm, and the change in dye concentration was monitored at this wavelength (Fig. 10). The suspensions were stirred in the dark for 60 min to reach adsorption–desorption equilibrium, which allowed us to evaluate the adsorption capacity of the powders. Pristine g-C_3N_4 showed the highest adsorption capacity, attributed to its dispersive, ZnO exhibited significantly lower adsorption, while the composites demonstrated intermediate values.

After the 60-min dark stage, the suspensions were irradiated. The photocatalytic activity of ZOCN2, ZOCN5, ZOCN10, and ZOCN20 composites, as well as pristine ZnO and g-C_3N_4, was investigated under simulated solar light for 90 min. Fig. 10a shows the change in MB concentration with irradiation time (C/C_0). The ZOCN10 composite exhibited the best photocatalytic performance, achieving about 95% degradation after 90 min. The other composites showed efficiencies ZOCN5 85%, ZOCN2

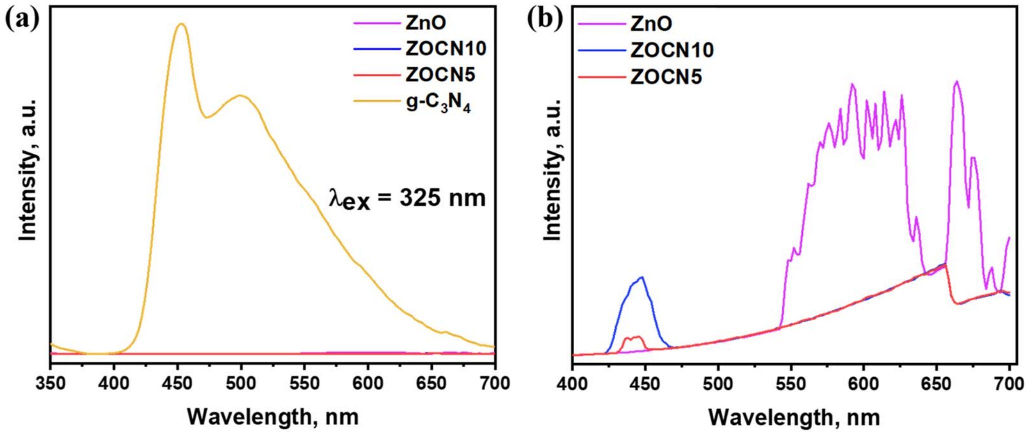

Fig. 9 Photoluminescence spectra of g-C_3N_4, ZnO, ZOCN5, ZOCN10 (a and b).

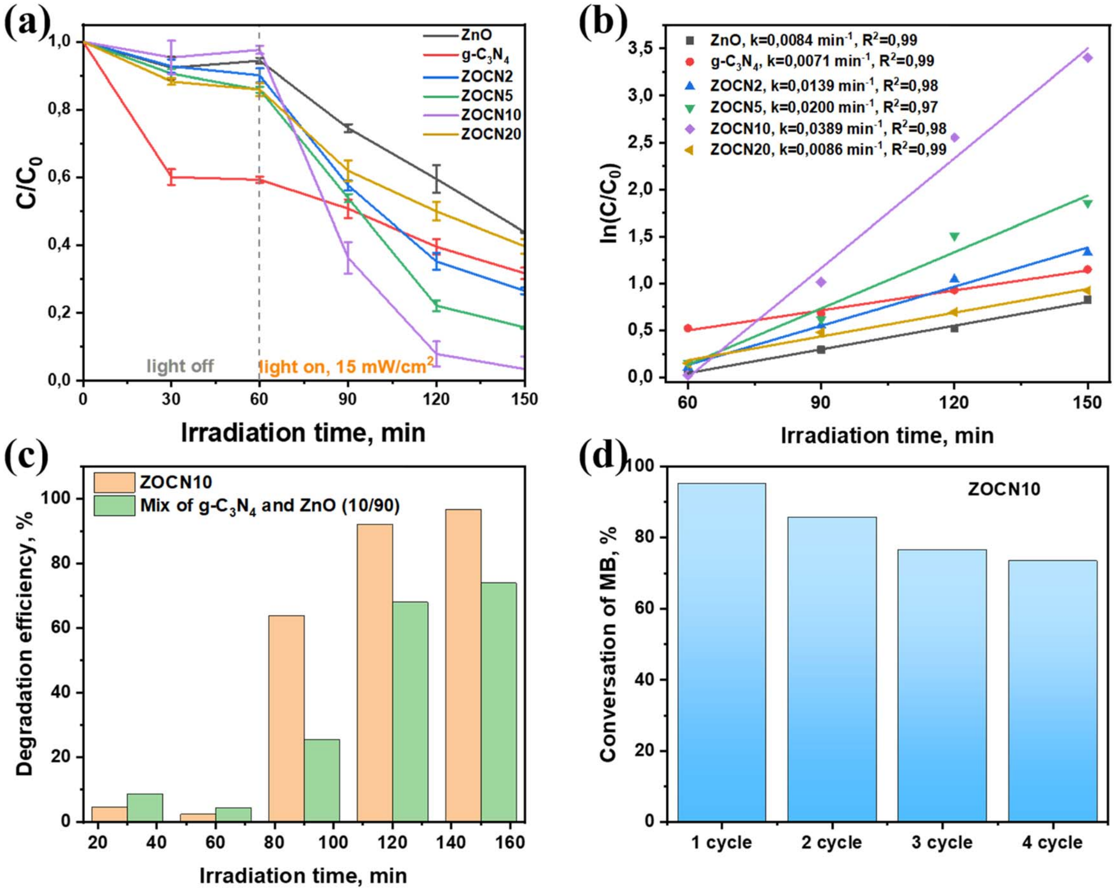

Fig. 10 Photocatalytic degradation of MB dye (a), pseudo-first-order kinetic model of MB dye in the presence of g-C_3N_4/ZnO composite (b), plot of evaluation of synergetic effect (c), recycling stability of ZOCN10 (d).

70% and ZOCN20 about 55%. Under the same conditions, pristine ZnO and g-C_3N_4 displayed considerably lower degradation efficiencies.

The bandgap energy determines the absorption edge and influences the photoexcitation of charge carriers; narrower bandgaps usually extend absorption to longer wavelengths, while wider bandgaps provide stronger redox potential. However, the difference between 2.98 eV (ZOCN10) and 2.92 eV (ZOCN20) is relatively small and cannot solely account for the observed differences in photocatalytic activity. In our case, the higher efficiency of ZOCN10 arises from a more favorable morphology and interfacial contact between ZnO and g-C_3N_4, which improves charge separation and suppresses electron–hole recombination. Thus, photocatalytic performance is governed not only by bandgap values but also by the synergistic effects of electronic structure, interfacial heterojunctions, and carrier dynamics.

3.4 Kinetics of the decomposition reaction

Analyzing the photocatalytic data, the kinetics of the decomposition reaction of the organic dye MB was quantitatively investigated using first-order pseudo-kinetics (Fig. 10b). To understand the kinetics of the MB photodegradation reaction in the presence of catalysts, the pseudo-first order eqn (3) was used to calculate the reaction rate constant:

$$\ln(C_0/C) = kt \tag{3}$$

where C_0 and C are the initial and final concentration of MB at a certain time interval, and k is the rate constant.

The calculated constant of the ZOCN10 composite is $k = 0.0389\ \text{min}^{-1}$, which is approximately 5,5 times greater than k (g-C_3N_4) $= 0.0071\ \text{min}^{-1}$ and 4,6 times greater than k (ZnO) $= 0.0084\ \text{min}^{-1}$, which indicates an increased photocatalytic activity of the ZOCN10 composite. The enhanced photocatalytic degradation efficiency of the ZOCN10 composite is mainly ascribed to its effective suppression of electron–hole recombination, facilitated by the strong interfacial contact between ZnO and g-C_3N_4 particles.

3.5 Evaluation of the synergistic effect

To compare the photocatalytic activity, mixtures of pure g-C_3N_4 and ZnO were prepared without mechanical activation. This mixtures were prepared in the same ratio as composite ZOCN10 that obtained mechanochemically. Comparing the results of degradation of MB (Fig. 10c), it can be concluded that in the presence of ZOCN10 nanocomposites, the concentration of organic dye decreases for 150 min and the solution discolors. However, when a simple mixture of g-C_3N_4 and ZnO was used, the degradation efficiency was comparatively reduced. This may be related to the formation of a heterostructure as a result of mechanochemical synthesis.

3.6 Cycling stability of ZOCN10

The stability of the synthesized catalysts was evaluated through recycling experiments (Fig. 10d). The ZOCN10 nanocomposite demonstrated good reusability, with only a slight reduction in apparent photocatalytic activity over four consecutive cycles. This decline can be primarily attributed to operational mass loss during kinetic sampling: in each cycle, 20–25% of the suspension volume is withdrawn for analysis, leading to a gradual reduction in the total catalyst recovered for subsequent runs. When the activity is normalized to the remaining catalyst mass, the performance remains essentially constant, confirming that the nanocomposites preserve their intrinsic photocatalytic efficiency. Moreover, although slight ZnO photocorrosion may occur, its impact is considered negligible under our experimental conditions, in agreement with previous studies on ZnO-based photocatalysts.[67] Overall, these findings highlight that the observed reduction is largely due to sample withdrawal rather than chemical degradation, and the nanocomposites exhibit good stability under repeated use.

Compared with representative g-C_3N_4/ZnO photocatalysts (Table 3), ZOCN10 delivers $k = 0.0389\ \text{min}^{-1}$ for MB (95% in 90 min at 10 mg L^{-1}), exceeding ultrasonic, high-energy ball-milled ($0.426\ \text{h}^{-1} \approx 0.0071\ \text{min}^{-1}$) and co-melting counterparts ($0.00461\ \text{min}^{-1}$). Notably, the solvent-free mechanochemical route affords a greener and readily scalable alternative while maintaining competitive kinetics relative to more complex microwave/ALD/two-step syntheses.

3.7 Effect of different factors on degradation efficiency over ZOCN10

Fig. 11(a–c) illustrates the photocatalytic degradation of MB over ZOCN10. Variation of the initial MB concentration (5, 10, 15 mg L^{-1}) at constant catalyst loading demonstrates an inverse dependence of degradation rate on concentration: the 5 mg L^{-1} solution degrades most efficiently (nearly complete removal within 120 min), 10 mg L^{-1} shows moderate performance, while 15 mg L^{-1} is least effective due to photon shielding and competitive adsorption at active sites; trend 5 > 10 > 15. The process is strongly affected by pH, reaching maximum efficiency at neutral conditions pH 7, decreasing at alkaline pH 9, and becoming least favorable in acidic medium pH 5, highlighting the role of surface charge effects on dye-catalyst interactions; trend pH 7 > pH 9 > pH 5. Increasing catalyst dosage (10 → 30 mg) accelerates the degradation, with 30 mg yielding the highest activity due to the abundance of active sites and enhanced radical formation; trend 30 > 20 > 10.

Our parametric tests (Fig. 11a–c) highlight the matrix sensitivity of ZOCN10: lower dye concentrations and near-neutral pH favor faster degradation, while acidic/alkaline conditions and higher pollutant loads reduce efficiency due to photon shielding and competitive adsorption. Recycling experiments (Fig. 10d) confirm the stability of the composites, with only minor losses attributable to sampling rather than chemical degradation. These results indicate strong potential for wastewater treatment, though certain limitations must be acknowledged, including pH sensitivity, possible ZnO photocorrosion, and challenges in recovering nanosized powders. Similar effects of co-ions (Cl^-, NO_3^-, SO_4^{2-}) and natural organics reducing efficiency have been systematically documented in real water matrices,[71] and related g-C_3N_4/metal oxide heterostructures have shown that activity remains significant even in wastewater.[72] Practical solutions, such as operation near neutral pH and immobilization or magnetic supports for catalyst recovery,[73] have been reported. Overall, our findings together with literature evidence confirm that ZOCN10 nanocomposite are promising, stable, and non-toxic materials for large-scale degradation of diverse organic pollutants.

Table 3 Photocatalytic efficiency of g-C_3N_4/ZnO and some previous photocatalysts

Catalyst	Synthesis method	Dye, C_0	Degradation efficiency, %	Light source	Rate constant, min^{-1}	Ref.
g-C_3N_4/ZnO catalysts						
ZnO/g-C_3N_4	Nebulizer spray pyrolysis	MB, 1×10^{-5} M	97%, 75 min	Sunlight	0.0489	3
ZnO/g-C_3N_4	High performance ball milling	RhB, 10 mg L^{-1}	51.3%, 2 h	Visible	0.0071	17
ZnO/g-C_3N_4	Ultrasonic dispersion	RhB, 20 mg L^{-1}	95.6%, 120 min	Sunlight	0.01957	37
g-C_3N_4@ZnO	Thermal atomic layer deposition	CEP 10 mg L^{-1}	98.9%, 60 min	Solar	0.0735	45
ZnO@g-C_3N_4	Two-step calculation	RhB, 5 mg L^{-1}	>90%, 50 min	Visible	0.0831	50
g-C_3N_4/ZnO	Co-melting-recrystallizing	MO, 10 mg L^{-1}	62%, 240 min	Visible	0.00461	56
ZnO-g-C_3N_4	Microwave irradiation	MB, 5 ppm	∼92%, 120 min	Sunlight	0.20	68
Other ZnO based catalyst						
g-C_3N_4/Ni–ZnO	Co-precipitation	MB, 10 mg L^{-1}	100%, 70 min	Sunlight	0.031	15
ZnS/ZnO	Mechanochemical	Orange II, 10 mg L^{-1}	90%, 420 min	Solar	0.00373	62
N–ZnO/g-C_3N_4	Ultrasonic assisted electrostatic self-assembly	NOR, 5 mg L^{-1}	96%, 90 min	Visible	0.0340	69
g-C_3N_4/Co@ZnO	Co-precipitation	MB, 10 mg L^{-1}	100%, 60 min	Solar	0.0250	70
g-C_3N_4/ZnO	Solid-state (mechanochemical)	MB, 10 mg L^{-1}	95%, 90 min	Solar	0.0389	This work

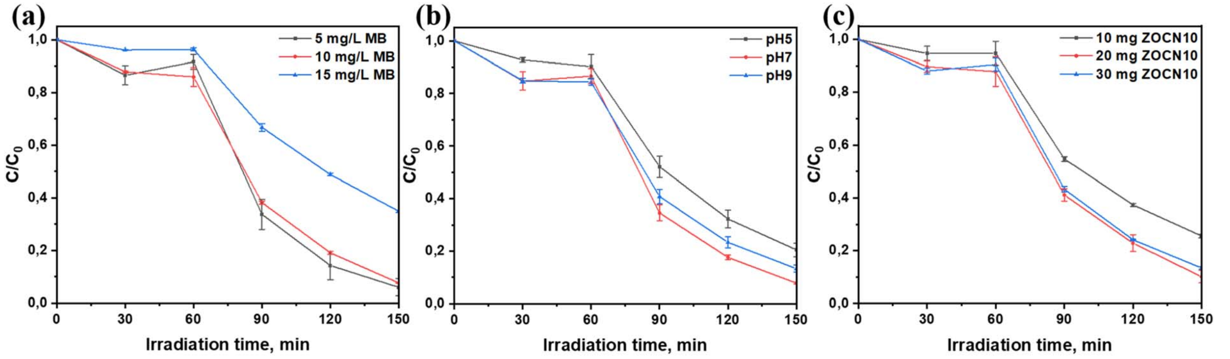

Fig. 11 Photocatalytic degradation of methylene blue (MB) over ZOCN10 under solar light irradiation: (a) initial dye concentration, (b) pH, (c) catalyst dosage.

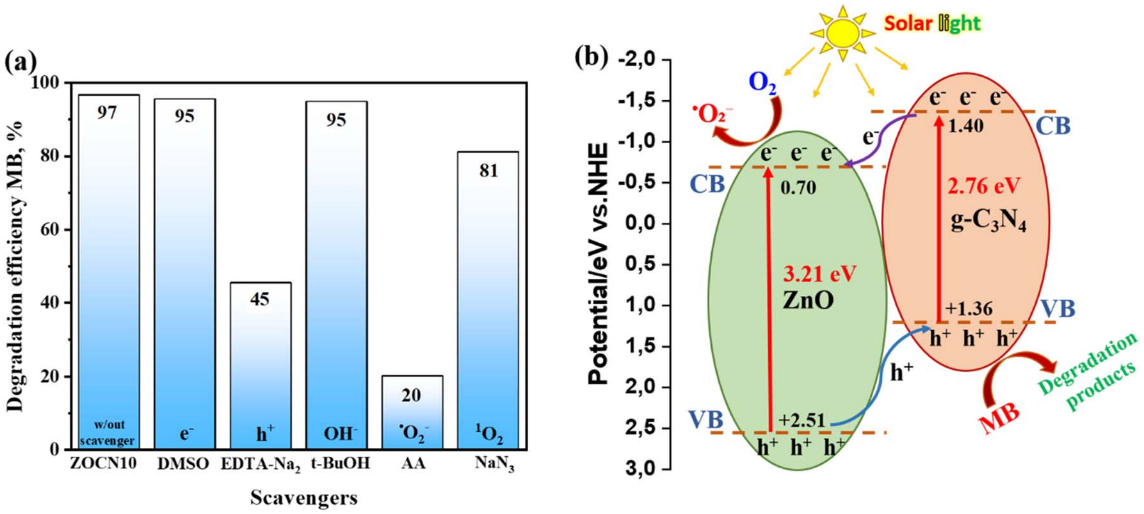

Fig. 12 Effect of scavengers on the photodegradation of MB over ZOCN10 photocatalyst (a), mechanism of MB dye degradation using ZOCN10 photocatalyst (b).

3.8 Mechanism of MB dye degradation

To elucidate the active species in MB degradation over ZOCN10 under solar light (Fig. 12a), scavenger experiments were performed using ascorbic acid (AA), sodium azide (NaN_3), *tert*-butanol (*t*-BuOH), dimethyl sulfoxide (DMSO), and disodium ethylenediaminetetraacetate (EDTA-Na_2) reagents was chosen as scavengers for superoxide radical ($^{\bullet}O_2^-$), singlet oxygen ($^1O_2$), hydroxyl ($^{\bullet}OH$), electron (e^-) and hole (h^+), respectively.[68,69] The degradation efficiency dropped most strongly in the presence of AA (20%), while a moderate decrease observed with EDTA-Na_2 (45%) and minor effect with NaN_3 (81%). The negligible changes with DMSO and *t*-BuOH indicate that e^- and hydroxyl radicals contribute weakly to the overall process.

XPS analysis together with Zn–N bonding evidences confirms the type-II heterojunction and efficient interfacial charge transfer in ZOCN10. Based on scavenger effects and optical band gap data, the degradation pathway of MB over ZOCN10 is proposed, as depicted in Fig. 12b. Under solar irradiation, photoexcited electrons in g-C_3N_4 (CB = −1.40 eV *vs.* NHE) transfer to the CB of ZnO (−0.70 eV), while holes migrate from the VB of ZnO (+2.51 eV) to the VB of g-C_3N_4 (+1.36 eV). Electrons accumulated on ZnO reduce dissolved oxygen to superoxide ($O_2 + e^- \rightarrow {}^{\bullet}O_2^-$),[74] which is the dominant reactive species responsible for MB degradation. Holes retained on g-C_3N_4 contribute secondarily *via* direct oxidation of adsorbed MB.[70]

4. Conclusion

g-C_3N_4/ZnO nanocomposites were synthesized by a solvent-free two-step route, combining thermal polymerization of melamine with mechanochemical integration of ZnO, followed by calcination. Structural and spectroscopic analyses confirmed the coexistence of both phases and strong Zn–N interfacial coupling, stabilizing the heterojunctions. Under simulated solar irradiation, the optimized ZOCN10 exhibited the highest activity with $k = 0.0389\ \text{min}^{-1}$, ∼95% MB removal within 90 min, outperforming pristine g-C_3N_4, ZnO 5.5 and 4.6 times. These results highlight the benefits of the scalable and solvent-free approach for producing efficient heterostructured photocatalysts.

Mechanistic studies revealed that superoxide radicals ($^{\bullet}O_2^{-}$) and holes dominate the degradation pathway. Their generation and utilization at the heterointerface explain the suppressed charge recombination and enhanced photocatalytic efficiency. Importantly, stability tests demonstrated that ZOCN10 retains a substantial portion of its activity across repeated cycles, indicating suitability for practical solar-driven wastewater treatment. Taken together, these findings establish a green, cost-effective, and scalable route for designing g-C_3N_4/ZnO composites with strong potential in environmental remediation.

Author contributions

Adina Zholdas: methodology, software, visualization, investigation, data curation, writing– original draft. Abylay Abilkhan: investigation, methodology, Oleg Rofman: writing – review & editing, investigation. Islam Rakhimbek: writing – review & editing, investigation. Daniyar Salikhov: writing – review & editing, investigation. Fail Sultanov: writing – review & editing. Batukhan Tatykayev: conceptualization, methodology, funding acquisition, supervision.

Conflicts of interest

The authors declare that there are no known financial or personal conflicts of interest that could have influenced the results or interpretation of the work presented in this paper.

Data availability

Additional raw data (XRD, FT-IR, TEM, SEM, XPS, and UV-vis spectra) are available from the corresponding author upon reasonable request.

The data supporting the findings of this study are available within the article and its supplementary information (SI). Supplementary information: preparation methods of g-C_3N_4/ZnO nanocomposites have been studied in detail and collected in Table S1, given in the Supplementary material and Supplementary Fig. S1 EDX results ZnO, g-C_3N_4, and ZOCN5, ZOCN10. See DOI: **https://doi.org/10.1039/d5ra06422h**.

Acknowledgements

This research has been funded by the Science Committee of the Ministry of Science and Higher Education of the Republic of Kazakhstan (grant no. AP27511547). We are grateful to Dr Zhandos Shalabayev for supporting our research. The authors gratefully acknowledge the NNLOT laboratory at the Faculty of Physics and Technology, Al-Farabi Kazakh National University, for providing SEM analysis of the catalysts, and Dr Madi Aitzhanov for his assistance with the XRD measurements. The authors also acknowledge the financial support from the INESS-2025 Organizing Committee and the Social Development Fund of Nazarbayev University, which covered the article processing charge for this publication. We also thank the Core Facilities laboratories of Nazarbayev University for assistance with sample characterization. We are also grateful to Dr Tugelbay Saparbek and Dr Natalya Khan for their assistance, and special thanks to Professor Raphael Schneider for consultations.

References

1 A. Kumar, *Int. J. Mater. Sci. Eng.*, 2017, **1**, 106–114.
2 H. Tong, S. Ouyang, Y. Bi, N. Umezawa, M. Oshikiri and J. Ye, *Adv. Mater.*, 2012, **24**, 229–251.
3 K. Ravichandran, K. Kalpana, R. Uma, E. Sindhuja and K. S. Seelan, *Mater. Res. Bull.*, 2018, **99**, 268–280.
4 J. Liu, X.-T. Yan, X.-S. Qin, S.-J. Wu, H. Zhao, W.-B. Yu, L.-H. Chen, Y. Li and B.-L. Su, *Catal. Today*, 2020, **355**, 932–936.
5 Y. Liu, H. Liu, H. Zhou, T. Li and L. Zhang, *Appl. Surf. Sci.*, 2019, **466**, 133–140.
6 D. Neena, M. Humayun, D. Bhattacharyya and D. Fu, *J. Photochem. Photobiol., A*, 2020, **396**, 112515, DOI: **10.1016/j.jphotochem.2020.112515**.
7 Y. He, Y. Wang, L. Zhang, B. Teng and M. Fan, *Appl. Catal., B*, 2015, **168–169**, 1–8.
8 N. Nie, L. Zhang, J. Fu, B. Cheng and J. Yu, *Appl. Surf. Sci.*, 2018, **441**, 12–22.
9 X. Pang, C. Cui, M. Su, Y. Wang, Q. Wei and W. Tan, *Nano Energy*, 2018, **46**, 101–109.
10 I. M. Sundaram, S. Kalimuthu and G. P. Ponniah, *Compos. Commun.*, 2017, **5**, 64–71.
11 A. Mathialagan, M. Manavalan, K. Venkatachalam, F. Mohammad, W. C. Oh and S. Sagadevan, *Opt. Mater.*, 2020, **100**, 109643.
12 A. Mirzaei, L. Yerushalmi, Z. Chen and F. Haghighat, *J. Hazard. Mater.*, 2018, **359**, 516–526.
13 R. Uma, K. Ravichandran, S. Sriram and B. Sakthivel, *Mater. Chem. Phys.*, 2017, **201**, 147–155.
14 S. Mondal and S. R. Wickramasinghe, *J. Membr. Sci.*, 2008, **322**, 162–170.
15 M. A. Qamar, S. Shahid, M. Javed, S. Iqbal, M. Sher, A. Bahadur, M. M. AL-Anazy, A. Laref and D. Li, *Colloids Surf., A*, 2021, **614**, 126176.
16 J.-Z. Kong, H.-F. Zhai, W. Zhang, S.-S. Wang, X.-R. Zhao, M. Li, H. Li, A.-D. Li and D. Wu, *Nanoscale Res. Lett.*, 2017, **12**, 526.
17 Q. Chen, H. Hou, D. Zhang, S. Hu, T. Min, B. Liu, C. Yang, W. Pu, J. Hu and J. Yang, *J. Photochem. Photobiol., A*, 2018, **350**, 1–9.
18 S. Abou Zeid and Y. Leprince-Wang, *Crystals*, 2024, **14**(7), 611.
19 A. Baig, M. Siddique and S. Panchal, *Catalysts*, 2025, **15**(2), 100.
20 K. Qi, B. Cheng, J. Yu and W. Ho, *J. Alloys Compd.*, 2017, **727**, 792–820.
21 J. Jiang, G. Zhang, Y. Yan, Y. Jiao, B. Sun and T. Cui, *J. Alloys Compd.*, 2024, **980**, 173655.
22 V. Kumari, A. Mittal, J. Jindal, S. Yadav and N. Kumar, *Front. Mater. Sci.*, 2019, **13**, 1–22.

23 B. Ghanbari Shohany and A. Khorsand Zak, *Ceram. Int.*, 2020, **46**, 5507–5520.
24 X. Jin, J. Chen, F. Chen, H. Duan, Z. Wang and J. Li, *Catalysts*, 2022, **12**(9), 981.
25 Y. M. Hunge, A. A. Yadav, S.-W. Kang, S. Jun Lim and H. Kim, *J. Photochem. Photobiol., A*, 2023, **434**, 114250.
26 S. K. Nadikatla, V. B. Chintada, T. R. Gurugubelli and R. Koutavarapu, *Molecules*, 2023, **28**(11), 4277.
27 N. Akter, T. Ahmed, I. Haque, M. K. Hossain, G. Ray, M. M. Hossain, M. S. Islam, M. A. Ali shaikh and U. S. Akhtar, *Heliyon*, 2024, **10**(10), 30602.
28 K. N. Van, H. T. Huu, V. N. Nguyen Thi, T. L. Le Thi, D. H. Truong, T. T. Truong, N. N. Dao, V. Vo, D. L. Tran and Y. Vasseghian, *Chemosphere*, 2022, **289**, 133120.
29 G. Mamba and A. K. Mishra, *Appl. Catal., B*, 2016, **198**, 347–377.
30 L. Bai, H. Huang, S. Yu, D. Zhang, H. Huang and Y. Zhang, *J. Energy Chem.*, 2022, **64**, 214–235.
31 K. R. Reddy, C. H. V. Reddy, M. N. Nadagouda, N. P. Shetti, S. Jaesool and T. M. Aminabhavi, *J. Environ. Manage.*, 2019, **238**, 25–40.
32 A. Alaghmandfard and K. Ghandi, *Nanomaterials*, 2022, **12**(2), 294.
33 X. Liu, R. Ma, L. Zhuang, B. Hu, J. Chen, X. Liu and X. Wang, *Crit. Rev. Environ. Sci. Technol.*, 2021, **51**, 751–790.
34 X. Chen, Y. Jin, P. Huang, Z. Zheng, L. P. Li, C. Y. Lin, X. Chen, R. Ding, J. Liu and R. Chen, *Appl. Catal., B*, 2024, **340**, 123235.
35 R. Rameshbabu, J. K. S. Paw, K. Ajaijawahar, V. Vinoth, S. Jadoun, N. Pugazhenthiran and T. S. Kiong, *J. Alloys Compd.*, 2024, **997**, 20–23.
36 B. Liu, C. Bie, Y. Zhang, L. Wang, Y. Li and J. Yu, *Langmuir*, 2021, **37**, 14114–14124.
37 K. Bi, X. Qin, S. Cheng and S. Liu, *Diam. Relat. Mater.*, 2023, **137**, 110143.
38 Q. Jiang, Y. Ma, P. Zhao, X. Li, Y. Shao and X. Xu, *Environ. Sci. Technol.*, 2025, DOI: **10.1021/acs.est.5c06061**.
39 J. Xiao, Y. Chen, C. Cai, S. Lai, L. Cheng, J. Zhang, W. Zhu, Y. Guo, M. Hou, L. Ma, W. Chen, X. Chen and C.-P. Wong, *Small*, 2025, **21**, 2503335.
40 X. Liu, X. Xu, H. Gan, M. Yu and Y. Huang, *Catalysts*, 2023, **5**, 848.
41 T. Nakagawa, S. Fujiwara, S. Shimoda, K. Suzuki, A. Fukuoka and T. Takada, *Chem. Phys. Lett.*, 2024, **850**, 141457.
42 P. Negro, F. Cesano, A. Damin, R. Brescia and D. Scarano, *J. Alloys Compd.*, 2024, **1002**, 175053.
43 P. Yang, J. Wang, G. Yue, R. Yang, P. Zhao, L. Yang, X. Zhao and D. Astruc, *J. Photochem. Photobiol., A*, 2020, **388**, 112169.
44 M. A. Qamar, M. Javed, S. Shahid and M. Sher, *Mater. Res. Bull.*, 2022, **147**, 111630.
45 N. Li, Y. Tian, J. Zhao, J. Zhang, W. Zuo, L. Kong and H. Cui, *Chem. Eng. J.*, 2018, **352**, 412–422.
46 Q. Zhong, H. Lan, M. Zhang, H. Zhu and M. Bu, *Ceram. Int.*, 2020, **46**, 12192–12199.
47 X. Gao, B. Yang, W. Yao, Y. Wang, R. Zong, J. Wang, X. Li, W. Jin and D. Tao, *Environ. Pollut.*, 2020, **257**, 113577.
48 Z. Xing, Y. Chen, C. Liu, J. Yang, J. Xu, Y. Situ and H. Huang, *J. Alloys Compd.*, 2017, **708**, 853–861.
49 S. Le, T. Jiang, Y. Li, Q. Zhao, Y. Li, W. Fang and M. Gong, *Appl. Catal., B*, 2017, **200**, 601.
50 L. Wang, C. Ma, Z. Guo, Y. Lv, W. Chen, Z. Chang, Q. Yuan, H. Ming and J. Wang, *Mater. Lett.*, 2017, **188**, 347–350.
51 H. Lv, G. Ji, Z. Yang, Y. Liu, X. Zhang, W. Liu and H. Zhang, *J. Colloid Interface Sci.*, 2015, **450**, 381–387.
52 J. Wang, Y. Xia, H. Zhao, G. Wang, L. Xiang, J. Xu and S. Komarneni, *Appl. Catal., B*, 2017, **206**, 406–416.
53 A. Akhundi and A. Habibi-Yangjeh, *Appl. Surf. Sci.*, 2015, **358**, 261–269.
54 Z. Wang, L. Zhang, Z. Liu, L. Sang, L. Yang and Q. Chen, *Nanoscale Res. Lett.*, 2017, **1**, 421.
55 W. Li, L. Fang, G. Qin, H. Ruan, H. Zhang, C. Kong, L. Ye, P. Zhang and F. Wu, *J. Appl. Phys.*, 2015, **117**, 145301.
56 X. Guo, J. Duan, C. Li, Z. Zhang and W. Wang, *J. Mater. Sci.*, 2020, **55**, 2018–2031.
57 F. Qiao, J. Wang, S. Ai and L. Li, *Sens. Actuators, B*, 2015, **216**, 418–427.
58 B. Zhu, P. Xia, W. Ho and J. Yu, *Appl. Surf. Sci.*, 2015, **344**, 188–195.
59 A. Zada, M. Khan, Z. Hussain, M. I. A. Shah, M. Ateeq, M. Ullah, N. Ali, S. Shaheen, H. Yasmeen, S. N. A. Shah and A. Dang, *Z. Phys. Chem.*, 2022, **236**, 53–66.
60 N. Mukwevho, N. Kumar, E. Fosso-Kankeu, F. Waanders, J. Bunt and S. S. Ray, *Desalin. Water Treat.*, 2019, **163**, 286–296.
61 G. Pan, J. Chen, K. Ge, L. Yang, F. Li, Z. Wang, S. Shi, X. Yang, Z. Zhou, A. Tang, W. Liu and Y. Sun, *J. Mater. Chem. C*, 2019, **7**, 4449–4458.
62 A. Oskenbay, D. Salikhov, O. Rofman, I. Rakhimbek, Z. Shalabayev, N. Khan, B. Soltabayev, A. Mentbayeva, M. Baláž and B. Tatykayev, *Ceram. Int.*, 2023, **49**, 32246–32260.
63 N. Khan, G. Burashev, A. Kadylbekova, T. S. Atabaev, Z. Bakenov, F. Sultanov, A. Mentbayeva and B. Tatykayev, *Sustain. Mater. Technol.*, 2024, **41**, e01063.
64 I. Khan, C. Wang, S. Khan, J. Chen, A. Khan, S. A. Shah, A. Yuan, S. Khan, M. K. Butt and H. Asghar, *Chin. J. Chem. Eng.*, 2023, **56**, 215–224.
65 S. Khan, A. Wang, J. Liu, I. Khan, S. Sadiq, A. Khan, W. Yaseen, S. Zaman, A. Mueed and Y. Miao, *Environ. Sci. Nano*, 2024, **12**, 1186–1201.
66 A. Altaf, I. Khan, A. Khan, S. Sadiq, M. Humayun, S. Khan, S. Zaman, A. Khan, R. A. Abumousa and M. Bououdina, *ACS Omega*, 2024, **9**, 34220–34242.
67 I. Khan, S. Sadiq, P. Wu, M. Humayun, S. Ullah, W. Yaseen, S. Khan, A. Khan, R. A. Abumousa and M. Bououdina, *Carbon Capture Sci. Technol.*, 2024, **13**, 100315.
68 Y. R. Girish, Udayabhanu, N. M. Byrappa, G. Alnaggar, A. Hezam, G. Nagaraju, K. Pramoda and K. Byrappa, *J. Hazard. Mater. Adv.*, 2023, **9**, 100230.
69 C. Zhang, M. Jia, Z. Xu, W. Xiong, Z. Yang, J. Cao, H. Peng, H. Xu, Y. Xiang and Y. Jing, *Chem. Eng. J.*, 2022, **430**, 132652.

70 M. A. Qamar, M. Javed, S. Shahid, S. Iqbal, S. A. Abubshait, H. A. Abubshait, S. M. Ramay, A. Mahmood and H. M. Ghaithan, *J. Environ. Chem. Eng.*, 2021, **9**, 105534.

71 S. Ahmad, M. Almehmadi, H. T. Janjuhah, G. Kontakiotis, O. Abdulaziz, K. Saeed, H. Ahmad, M. Allahyani, A. Aljuaid, A. A. Alsaiari, J. Muhammad and I. Khan, *Water*, 2023, **15**(1), 175.

72 J. Ni, W. Wang, D. Liu, Q. Zhu, J. Jia, J. Tian, Z. Li, X. Wang and Z. Xing, *J. Hazard. Mater.*, 2021, **408**, 124432.

73 Y. Wu, X. Chen, Y. Han, D. Yue, X. Cao, Y. Zhao and X. Qian, *Environ. Sci. Technol.*, 2019, **53**, 9081–9090.

74 Z. Zhang, Y. Sun, Y. Wang, Y. Yang, P. Wang, L. Shi, L. Feng, S. Fang, Q. Liu, L. Ma, S. Peng and T. Wang, *Ceram. Int.*, 2022, **48**, 3293–3302.